

Hilbert Space Fragmentation and Exact Scars of Generalized Fredkin Spin Chains

Christopher M. Langlett¹ and Shenglong Xu^{1,*}

¹*Department of Physics & Astronomy, Texas A&M University, College Station, Texas 77843, USA*

In this work, based on the Fredkin spin chain, we introduce a family of spin-1/2 many-body Hamiltonians with a three-site interaction featuring a fragmented Hilbert space with coexisting quantum many-body scars. The fragmentation results from an emergent kinetic constraint resembling the conserved spin configuration in the 1D Fermi-Hubbard model in the infinite onsite repulsion limit. To demonstrate the many-body scars, we construct an exact eigenstate that is in the middle of the spectrum within each fractured sub-sector displaying either logarithmic or area-law entanglement entropy. The interplay between fragmentation and scarring leads to rich tunable non-ergodic dynamics by quenching different initial states that is shown through large scale matrix product state simulations. In addition, we provide a Floquet quantum circuit that displays non-ergodic dynamics as a result of sharing the same fragmentation structure and scarring as the Hamiltonian.

Introduction – In a closed quantum system described by a generic interacting Hamiltonian, a simple initial state evolves unitarily in an exponentially large Hilbert space along with rapid entanglement growth. Simultaneously, the local state density matrix converges to the thermal ensemble independent of the initial states details, a process called quantum thermalization—a direct consequence of the Eigenstate Thermalization Hypothesis(ETH) [1–5]. ETH is known to be violated in the presence of strong disorder leading to many-body localization causing entanglement growth to be suppressed and retention of the initial state [6–10].

Experimental progresses in various quantum platforms such as ion traps, Rydberg atom arrays, and superconducting qubits have enabled unprecedented control over probing long time dynamics of large scale many-body systems up to 53-qubits [11–16]. This provides an exciting opportunity to study thermalization and when it is violated, as well as, engineer non-equilibrium phases of matter. One important discovery of this renaissance is the late time coherent oscillations in a 51-qubit Rydberg array quenched from a Néel state [17]. Providing an example of weak ETH violation, this discovery has coalesced into an extensive study of quantum many-body scars that has unveiled a connection to emerging Lie algebras, lattice gauge theory, and Floquet circuits [18–31].

There has been a large effort to find other counterexamples to ETH. It has been shown that non-thermal behavior can arise due to combinations of conserved quantities such as charge and dipole [32–34], or charge and domain-wall number [35]. The interplay of these conserved quantities leads to the Hilbert space fracturing into exponentially many disconnected sub-sectors. This phenomenon, dubbed Hilbert space fragmentation, is found in a wide range of models [36–39], and has also been experimentally observed in the disorder-free tilted 1D Fermi-Hubbard model realized using optical lattices [40]. As a result of the new Hilbert space structure, the standard notion of thermalization does not occur. However,

it is found that an initial state prepared in a large sub-sector thermalizes within that sub-sector [41], with the exception to integrable sub-sectors. Here the eigenstates obey Krylov-restricted ETH.

What remains largely unexplored is whether the fragmented sub-sectors can host quantum many-body scars that weakly violate the Krylov-restricted ETH? If yes, then the combination of fragmentation and many-body scars may open a new window to richer non-equilibrium phenomena [42]. In this work, we provide a definite answer by introducing a quantum many-body model based on the deformed Fredkin spin-chain [43–47] that displays a coexistence of fragmentation and exact many-body scars. We show through embedding the ground state [48, 49] into the middle of the spectrum the Hilbert space splits into exponentially many disconnected sub-sectors. An exact ETH-violating eigenstate displaying sub-volume law entanglement entropy is found for *every* sub-sector with others revealed by numerics. Due to the fragmentation and many-body scar states, the Hamiltonian displays rich tunable non-ergodic dynamics presented through large scale tensor network simulations. Interestingly, the non-ergodic dynamics is closely related to domain-wall melting and propagation in the XXZ spin-chain with a boundary magnetic field. Furthermore, we substantiate our results by designing a Floquet quantum circuit that hosts the same dynamical properties.

Model – The simplest version of the model we introduce is the dressed Heisenberg chain,

$$H = \sum_{i=2}^{N-2} \sigma_{i-1}^z (1 - \vec{\sigma}_i \cdot \vec{\sigma}_{i+1}) + (1 - \vec{\sigma}_i \cdot \vec{\sigma}_{i+1}) \sigma_{i+2}^z \quad (1)$$

with the Heisenberg interaction dressed by the Pauli-z operator, σ_i^z . The Hamiltonian above conserves total magnetization, $S_z = \sum_i \sigma_i^z$. The spectrum of Eq. (1) is symmetric around zero due to anti-commuting with the operator, $C = \prod_i \sigma_i^x$ [50]. The off-diagonal term of the Hamiltonian in Eq. (1) acts on states through the controlled-SWAP spin moves,

$$|\uparrow\uparrow\downarrow\rangle \longleftrightarrow |\uparrow\downarrow\uparrow\rangle, \quad |\downarrow\uparrow\downarrow\rangle \longleftrightarrow -|\uparrow\downarrow\downarrow\rangle. \quad (2)$$

* slxu@tamu.edu

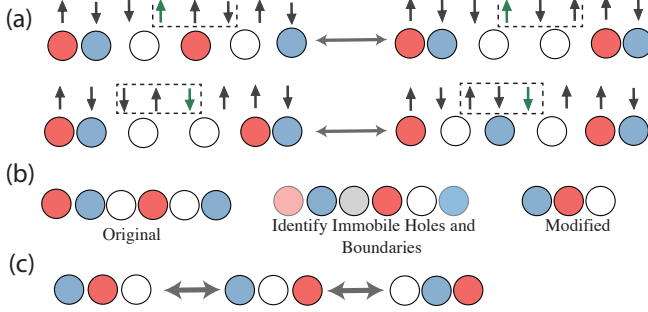


FIG. 1. (a) Visualization of the controlled-SWAP spin flip in Eq. 2 on original spins and the effective particle picture. The control bit is highlighted in green. The spin flip corresponds to hole hopping through the particles. (b) Immobile holes, (•), and left(right) boundary particles denoted, (••), are inert and removed leaving a modified sequence. (c) The spin flips correspond to nearest-neighbor hopping of the holes in the modified sequence.

From destructive interference between the spin moves there is also $U(1)$ conservation of domain-wall number, $n_{dw} = \sum_i \sigma_i^z \sigma_{i+1}^z$. The interplay between S_z and n_{dw} leads to the Hilbert space fragmentation [35]. For example, the Néel state, $|\uparrow\downarrow\cdots\uparrow\downarrow\rangle$ and domain-wall state, $|\uparrow\cdots\uparrow\downarrow\cdots\downarrow\rangle$, are both eigenstates corresponding to one-dimensional sub-sectors.

The above model is generalized to a family of frustration free Hamiltonians parameterized by q , defined to be

$$H(q) = \frac{4}{q} \sum_{i=2}^{N-2} \left(P_{i-1}^{\uparrow} |\Phi\rangle \langle \Phi|_{i,i+1} - |\Phi\rangle \langle \Phi|_{i,i+1} P_{i+2}^{\downarrow} \right), \quad (3)$$

where the state $|\Phi\rangle_{i,i+1} = |\uparrow\downarrow\rangle - q|\downarrow\uparrow\rangle$ is on site i and $i+1$. At $q=1$, the Hamiltonian recovers Eq. (1). The Hamiltonian is closely related to the deformed Fredkin chain [43, 44] where the two terms in Eq. (3) are both positive. The Fredkin chain is known to have a solvable ground state constructed as a superposition of Dyck walks exhibiting unique entanglement properties [43, 44]. More importantly, we construct an exact eigenstate with sub-volume law entanglement entropy for each sub-sector which due to the frustration free form of Eq. (3) is valid for arbitrary q . As a result, the model described in Eq. (3) exhibits fragmentation with coexisting quantum many-body scars leading to a rich class of non-ergodic dynamics, which we elaborate on below.

Fragmentation and Effective Hamiltonian – To characterize the fragmentation structure, we develop an effective description of Eq. (3) in close analogy with the 1D Fermi-Hubbard model at infinite- U , where the electron spin configuration is conserved. Given a state in the spin representation we first map the sequence, $|\downarrow\uparrow\rangle \rightarrow |\circ\rangle$, and then map the remaining individual spins to colored particles, $|\uparrow(\downarrow)\rangle \rightarrow |\bullet(\bullet)\rangle$. Consequently, the spin moves, Eq. (2), produce a kinetic constraint forbidding red(blue) particle exchange. Analogous to the electrons spin config-

uration of the infinite- U Hubbard model, the color order of the particles is a Hamiltonian invariant. The fractured sub-spaces are constructed by all spin states corresponding to the same color sequence. While maintaining this constraint, the spin flips, Eq. (2), correspond to particle hopping, shown in Fig. 1(a). There is a further constraint that at least one hole sits between a left domain of blue particles and a right red domain. The configuration in the particle picture has the form, $\bullet\cdots\bullet\circ\cdots\bullet$, or $\downarrow\cdots\downarrow\uparrow\uparrow\cdots\uparrow$ in the spin representation, which is frozen as a result of conservation of n_{dw} and S_z . This constraint can be accommodated by removing one hole between each pair of the blue and red domains. The same situation occurs for the holes between the left(right) boundary and a red(blue) domain (see appendix A). In addition, the red(blue) particle on the left(right) boundary is immobile as well because the Hamiltonian conserves the boundary spins. Removing these immobile degrees of freedom (Fig. 1(b)), the action of spin flips Eq. (2) are understood as nearest-neighbor hopping of the holes through colored particles with fixed color order shown in Fig. 1(c). We denote the number of mobile red(blue) particles as $n_{\bullet}(n_{\circ})$ and mobile hole number as n_{\circ} . The dimension of each fractured sub-sector is simply the binomial number, $\text{dim} = \binom{n_{\bullet} + n_{\circ} + n_{\circ}}{n_{\circ}}$. The frozen sub-sectors arise when either $n_{\bullet} + n_{\circ} = 0$ or $n_{\circ} = 0$. The largest sub-sector occurs when $\gamma = n_{\circ}/N = (5 - \sqrt{5})/10$ with $\text{dim} \sim ((1 + \sqrt{5})/2)^N$, exponentially smaller than the total Hilbert space 2^N .

We further construct an effective Hamiltonian equivalent to Eq. (3) that operates on the particle degrees of freedom specified through the color sequence and hole number. The effective Hamiltonian involves nearest-neighbor hopping, staggered potential and nearest-neighbor interaction

$$H(q) = -t \sum_i \left(c_{i,\bullet}^{\dagger} c_{i+1,\bullet} - c_{i,\bullet}^{\dagger} c_{i+1,\bullet} \right) + h.c. \quad (4)$$

$$+ V(q) \sum_i (n_{i,\bullet} - n_{i+1,\bullet})^2 - (n_{i,\bullet} - n_{i+1,\bullet})^2$$

$$+ h(q) \sum_i (n_{i,\bullet} - n_{i+1,\bullet}) + (n_{i,\bullet} - n_{i+1,\bullet}).$$

where $c_{i,\bullet(\circ)}$ is the annihilation operator of a red(blue) particle at site i , and $n_{i,\bullet(\circ)}$ counts the on-site color particle number. Importantly, the on-site double occupied states are projected out from the Hilbert space, similar to the on-site infinite repulsion limit of the Hubbard model, leading to the conserved color order of the particles that labels each fractured sub-sector. Here the hopping parameter, $t = 4$, nearest-neighbor interaction, $V(q) = 2(1/q + q)$, and onsite potential, $h(q) = 2(1/q - q)$. Note that the onsite potential cancels in the bulk leaving only a boundary term, $H_{\partial} = h(q)(n_{1,\bullet} + n_{1,\bullet} - n_{L,\bullet} - n_{L,\bullet})$. Through a Jordan-Wigner transformation, Eq. (4) is equivalent to an XXZ ladder with ferromagnetic and anti-ferromagnetic coupling on each leg with the constraint that the two spins on each rung cannot be up simultane-

ously.

Thermalization and Integrability – The color order is central to the interplay between chaos and integrability. When the sequence is monochromatic, the effective Hamiltonian is equivalent to the integrable XXZ chain with an easy-axis anisotropy parameter, $\Delta = V(q)/4 \geq 1$. On the other hand, a generic color sequence is expected to display Krylov-restricted thermalization [41]. As an example of the different behaviors we focus on two sub-sectors (Fig. 2(a) inset) with the same dimension. First, we study the level statistics quantified with the average ratio parameter, $r_n = \min(\delta^n, \delta^{n+1})/\max(\delta^n, \delta^{n+1})$ [6, 51, 52]. We find for the single color, $\langle r \rangle \approx 0.386$, as expected for an integrable system. On the other hand, for the sub-sector characterized by, $\bullet\bullet\cdots\bullet\bullet\cdots\bullet$, $\langle r \rangle \approx 0.529$ which is near the Wigner-Dyson result, indicating chaos. We further checked the sub-sector remains Wigner-Dyson for $q \in [0.5, 2.0]$ (see Fig. 5).

Exact many-body scars – The most remarkable feature of the system is that each fractured Hilbert space hosts one exact eigenstate that can be analytically constructed for arbitrary q

$$|\Psi(q)\rangle = \frac{1}{\mathcal{N}(q)} \sum_i^{\dim} e^{-\log(q)\hat{\mathcal{P}}/2} |\psi\rangle_i, \quad (5)$$

where $\hat{\mathcal{P}} = \sum_i i\sigma_i^z$ is the dipole operator in the original spin representation, the summation is over all states in the computational basis in each fractured sub-sector, with the normalization factor, $\mathcal{N}(q)^2 = \text{tr}(q^{-\hat{\mathcal{P}}})$. When $q = 1$, the eigenstate in each fractured sub-sector generalizes a Rokhsar-Kivelson state to the middle of the spectrum [53–55]. To verify Eq. (5) is an eigenstate of the Hamiltonian Eq. (3), notice that $\exp(-\log(q)\hat{\mathcal{P}}/2) \prod_{i=1}^N |\uparrow + \downarrow\rangle_i$ is a product state that is annihilated by each projector in the Hamiltonian. This indicates that this product state projected into each fragmented sub-sector must also be zero energy eigenstate. Due to the wavefunction structure and conservation of holes, the half-chain entanglement S of Eq. (5) is upper bounded by $\log(\min(2n_o + 1, N - 2n_o + 1))$. This is also confirmed by explicit construction of a matrix product state of the exact state shown in appendix C. As a result, S can scale at most logarithmically with N , in direct violation of ETH which predicts the entanglement entropy for middle spectrum eigenstates to be volume law. Therefore, $|\Psi(q)\rangle$ is scarred within chaotic sub-sectors such as the one associated with, $\bullet\bullet\cdots\bullet\bullet\cdots\bullet$ [56].

We analyze the entanglement scaling of $|\Psi(q)\rangle$ as a function of q , $n_\bullet + n_\circ$ and n_o see appendix C. When $n_\bullet + n_\circ$ or n_o stay constant with $N \rightarrow \infty$. Utilizing a large N analysis in the sub-sector, $\bullet\bullet\cdots\bullet\bullet\cdots\bullet$, when $n_\bullet + n_\circ$ and n_o scale linearly with system size, $S \sim \log(N)$ at $q = 1$, however, as q increases, S rapidly approaches zero, see Fig. 2(b). The reason is that $|\Psi(q)\rangle$ is limiting towards a product state with the largest dipole amplitude. When $q < 1$, the eigenstate is approximately a

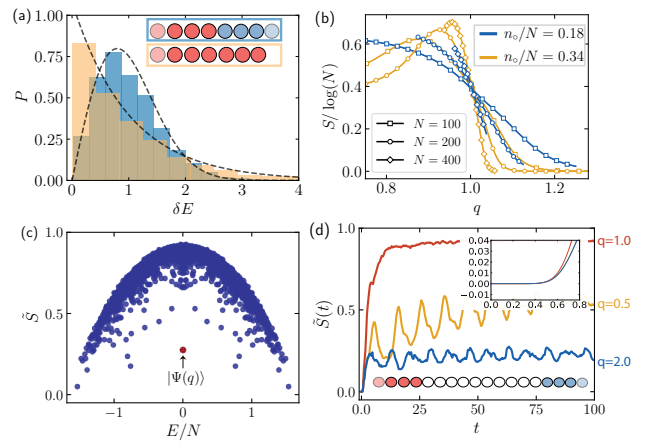


FIG. 2. (a) At $q = 1$, two fractured sub-sectors display Wigner-Dyson and Poisson Many-body level statistics. Each sub-sector contains 10 holes with $\dim = 8008$ and are labeled by the color sequence sketched in the figure. (b) The scaling of the Rényi entropy of the exact eigenstate from the MPS construction for the chaotic sub-sector. The ratio is fixed as N increases from 100 to 400. The entanglement entropy scales as $\log(N)$ at $q = 1.0$, but decays to zero for $q > 1$. For $q < 1$, the scaling depends on the ratio n_o/N . (c) Half-chain normalized Rényi entropy, \tilde{S} , of each eigenstate in the chaotic sub-sector. The low lying states, including the exact eigenstate in Eq. (5) highlighted in red, indicate quantum many-body scars. (d) Dynamics of \tilde{S} for the initial state within the chaotic sub-sector using exact diagonalization. Here $N = 28$ with $n_o = 10$. In the early time, \tilde{S} stays zero until $t \sim 0.6$, shown in the inset. The late time behavior depends on the value of q .

superposition of $(n_o + 1)$ states with the smallest dipole moment amplitude. Depending on whether $n_o/N > 1/4$, the state exhibits area or logarithmic entanglement. This analysis is confirmed by direct calculation of S using MPS for large system size up to $N = 400$, illustrated in Fig. 2(b), which reveals a change of entanglement scaling at $q = 1$. We further study the eigenstate entanglement entropy normalized as $\tilde{S} = S/\log(\sqrt{\dim})$ using exact diagonalization for $N = 28$, shown in Fig. 2(c). Intriguingly, the figure also clearly demonstrates outlying states significantly below the ETH-like curve, indicating multiple many-body scarred states distinct from Eq. (5).

Dynamics – These scarred states manifest themselves in the quantum dynamics of special initial states. We identify the product state, $|\psi\rangle = |\bullet\bullet\cdots\bullet\bullet\cdots\bullet\rangle$, in the effective picture with the largest dipole moment amplitude due to the high overlap with the exact eigenstate for $q > 1.0$. This state has zero energy density and by ETH should be thermal. We study the half-chain entanglement dynamics for, $q = 0.5, 1.0$ and 2.0 , with the system prepared in this state. A first indication of atypical dynamics is a plateau of zero-entanglement for $t < 0.6$, present for each q and absent in otherwise random states, inset Fig. 2(d). This follows from the time-

scale of the rightmost red particle and leftmost blue particle to propagate to the center and scatter. When $q = 1.0$, \tilde{S} , quickly saturates, while at $q = 2.0$, the entanglement remains finite at $\tilde{S} \sim 0.2$, far below the thermal expectation due to a high overlap with the exact eigenstate. Late-time coherent oscillations arise at $q = 0.5$ and are absent at $q = 2.0$ despite the effective Hamiltonian differing only by H_∂ .

In the following, we show that the various non-ergodic dynamics can be understood intuitively as the interplay between domain wall dynamics and the boundary term in the effective Hamiltonian Eq. (4). Moreover, utilizing MPS simulations we show the non-ergodic dynamics is not a finite-size effect but persists for long spin-chains. The state, $|\psi\rangle$, contains two domain walls between the red(blue) particle domain and the hole domain. In the spin representation the domain walls are between fully polarized and Néel configurations. During unitary evolution, the domain walls melt independently before meeting at the center, Fig. 3(a). The effective Hamiltonian structure suggests the domain wall melting is related to the XXZ chain for $\Delta \geq 1$ with an additional boundary term that complicates the dynamics. For the XXZ chain, the domain wall state is near the ground state. It was demonstrated when $\Delta = 1.0$ melting is super-diffusive [57], while nearly static when $\Delta > 1.0$ [58].

Quench dynamics of $|\psi\rangle$ are studied with the time-dependent variational principle (TDVP) [59, 60]. First, we consider a chain of length $N = 56$ with $n_\bullet = n_\circ = 7$ with $n_o = 20$, where small system exact diagonalization is found in appendix E. Fig. 3 plots the space-time dynamics of $\langle\sigma_i^z(t)\rangle$ in the spin representation which displays domain wall melting at $q = 1.0$ but static at $q = 2.0$, similar to the XXZ chain. While at $q = 0.5$ the domain walls do not melt, the two domains do however slowly leave the boundary unlike at $q = 2.0$. This difference becomes more prominent for shorter domains, shown in Fig. 3(b). We emphasize that the bulk terms in the effective Hamiltonian are the same for $q = 0.5$ and $q = 2.0$. The difference between the dynamics arises from the boundary term H_∂ , which is opposite for the two cases. The boundary term changes the energy cost of moving the domain from $2(q+1/q)$ to $4q$, a significant reduction for $q < 1.0$. The consequence is ballistic domain propagation illustrated in Fig. 3(b) for $q = 0.5$. In contrast, for $q > 1.0$ the boundary increases the energy cost, rendering the domain static. This also explains the entanglement growth in Fig. 2(d) between $q = 0.5$ and $q = 2.0$, where the coherent oscillations for $q = 0.5$ are attributed to domain scattering. This mechanism also suggests non-ergodic dynamics also occur for initial states with the red(blue) domains of different length and at different positions. As an example, we study the quench dynamics of another initial state $|\bullet\circ\cdots\circ\bullet\cdots\bullet\circ\cdots\bullet\rangle$ which also has zero energy density, see Fig. 3(c) and (d). The nearest-neighbor energy cancels in the configuration $\cdots\bullet\circ\bullet\cdots$ which permits collective hopping of the red domain without changing the configuration energy. As

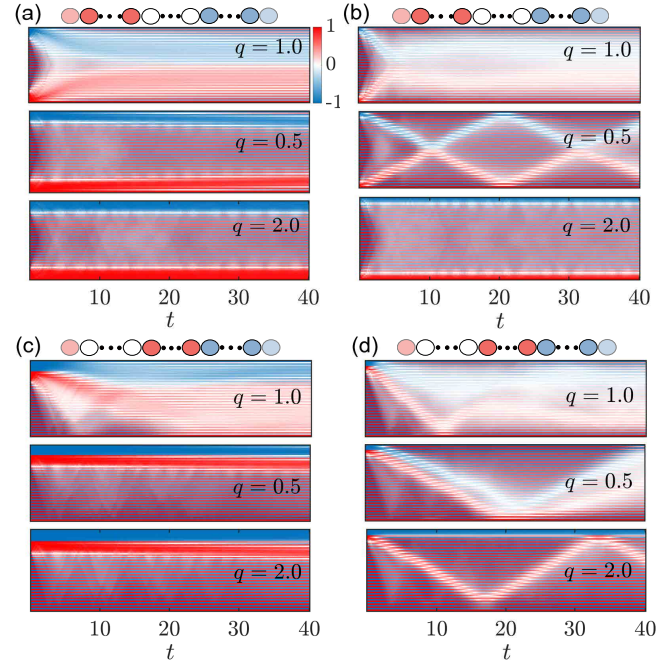


FIG. 3. Dynamics of $\langle\sigma_i^z(t)\rangle$ at $q = 0.5, 1.0, 2.0$ for two different domain-wall initial states for $N = 56$. We consider two different domain lengths. In (a) and (c), $n_\bullet = n_\circ = 7$ and $n_o = 20$. In (b) and (d), $n_\bullet = n_\circ = 3$ and $n_o = 24$. We simulate the dynamics using TDVP-MPS with bond dimension 48 and time step $dt = 0.04$ for $t = 40$. Technical details of TDVP and result from exact diagonalization can be found in appendix E and D respectively.

a result, the red domain always displays ballistic propagation, while at $q = 0.5$ the blue domain moves from an energy reduction due to H_∂ , similar to $|\psi\rangle$ at $q = 0.5$.

Quantum Circuit – We extend the Hamiltonian in Eq. (3) to a unitary Floquet quantum circuit sharing the same properties. The circuit contains three-site unitary gates which has immediate implementation [61–64]. The Floquet operator takes the form

$$U_T(\xi, q) = \prod_{i=1}^3 \prod_{l=1}^3 U_{3i+l-3}^\uparrow U_{3i+l}^\downarrow$$

$$U_i^\uparrow = e^{\frac{-4i\xi}{q} (P_i^\uparrow |\Phi\rangle\langle\Phi|_{i+1, i+2})}, \quad U_i^\downarrow = e^{\frac{+4i\xi}{q} (P_i^\downarrow |\Phi\rangle\langle\Phi|_{i-2, i-1})}. \quad (6)$$

The parameter $\xi \in [0, \xi_o]$ where $\xi_o(q) = q\pi/(2 + 2q^2)$ since $U_T(\xi + \xi_o, q) = U_T(\xi, q)$. The circuit configuration and gate decomposition are shown in appendix F. When $\xi \rightarrow 0$ the circuit is the Trotterization of the Hamiltonian dynamics. For general ξ , the circuit exhibits the same fractured Hilbert space as the Hamiltonian and importantly the scar state in Eq. (5) remains an eigenstate of the Floquet operator. As a result, we expect similar non-ergodic dynamics to occur in the Floquet dynamics whereas typical states are expected to thermalize to infinite temperature. In addition, at the point $(\xi = \pi/8, q = 1.0)$, Eq. (6), is a classical cellular au-

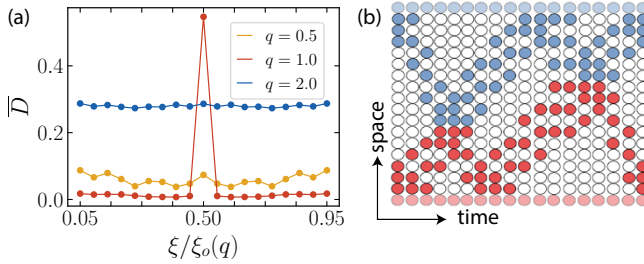


FIG. 4. (a) Dynamics of the Floquet unitary circuit at $(\xi = \pi/8, q = 1.0)$. (a) Thermal deviation, \bar{D} within the sub-sector $N = 28$, $n_\bullet = n_\circ = 3$ and $n_\circ = 10$ prepared in the state with the largest dipole amplitude. We time average $\langle \sigma_i^z(t) \rangle$ over late-driving periods between 3200 and 3600. For $q = 1.0$ there is a disparate point at $\xi/\xi_0(q) = 0.5$ corresponding to the classical point. (b) Dynamics of the Floquet unitary circuit at the classical cellular automaton point for one period of the classical trajectory.

tomaton which has recently received a reviving interest in non-equilibrium dynamics [65–67]. In our case, the update rules are given by the Fredkin gate

$$U_i^\uparrow = e^{-\frac{i\pi}{4} P_i^\uparrow (1 - \vec{\sigma}_{i+1} \cdot \vec{\sigma}_{i+2})}, \quad U_i^\downarrow = e^{\frac{i\pi}{4} P_i^\downarrow (1 - \vec{\sigma}_{i-1} \cdot \vec{\sigma}_{i-2})}. \quad (7)$$

We quantify the deviation of the dynamics from thermalization by $D(t) = \frac{1}{N} \sum_i |\langle \sigma_i^z(t) \rangle - \langle \sigma_i^z \rangle_{\text{th}}|$. We further average $D(t)$ over late-time driving periods between 3200 to 3600 periods. We again choose the state with the largest dipole amplitude as the initial state. The result, denoted \bar{D} for different ξ and q is shown in Fig. 4(a), demonstrates that even driving maintains the non-thermal properties of the system. The large peak at $q = 1.0$ and

$\xi/\xi_0(q) = 0.5$ is attributed to the classical point, showing the maximal deviation from thermalization. The corresponding dynamics in the effective picture is plotted in Fig. 4(b), demonstrating classical motion of the particles.

Conclusion – In this work we introduced a spin-1/2 Hamiltonian with nearest and next-nearest neighbor interactions that exhibits a fractured Hilbert space hosting chaotic and integrable sub-sectors. Each sub-sector is uniquely labeled by a invariant color sequence, that resembles the spin configuration in the infinite- U Hubbard model. We construct an exact eigenstate with sub-volume law entanglement which violates Krylov-restricted ETH in ergodic sub-sectors. By focusing on a specific chaotic sub-sector, we find quenching from a domain wall leads to rich non-ergodic dynamics related to domain wall melting and propagation. In connection with recent advancements in noisy intermediate quantum devices, we also provide a quantum circuit which mimics the dynamical properties of the Hamiltonian. From the conjunction of fragmentation and many-body scars our system enables control over various non-equilibrium phenomena by simply changing the initial states. This work also leads to many interesting future directions such as studying color sequences with periodic or quasi-periodic structure, quenched disorder that preserves the exact state and extending the model to the colored Fredkin spin chain.

Acknowledgement – S.X and C.M.L thank Lakshya Agarwal, Zhi-Cheng Yang and Brian Swingle for helpful comments on the manuscript. The numerical simulation in this work was conducted with the advanced computing resources provided by Texas A&M High Performance Research Computing.

[1] J. M. Deutsch, Quantum statistical mechanics in a closed system, *Phys. Rev. A* **43**, 2046 (1991).

[2] M. Srednicki, Chaos and quantum thermalization, *Phys. Rev. E* **50**, 888 (1994).

[3] M. Rigol, V. Dunjko, and M. Olshanii, Thermalization and its mechanism for generic isolated quantum systems, *Nature* **452**, 854 (2008).

[4] H. Kim, T. N. Ikeda, and D. A. Huse, Testing whether all eigenstates obey the eigenstate thermalization hypothesis, *Phys. Rev. E* **90**, 052105 (2014).

[5] M. Rigol and M. Srednicki, Alternatives to eigenstate thermalization, *Phys. Rev. Lett.* **108**, 110601 (2012).

[6] V. Oganesyan and D. A. Huse, Localization of interacting fermions at high temperature, *Phys. Rev. B* **75**, 155111 (2007).

[7] R. Nandkishore and D. A. Huse, Many-Body Localization and Thermalization in Quantum Statistical Mechanics, *Annual Review of Condensed Matter Physics* **6**, 15 (2015).

[8] M. Serbyn, Z. Papić, and D. A. Abanin, Local Conservation Laws and the Structure of the Many-Body Localized States, *Phys. Rev. Lett.* **111**, 127201 (2013).

[9] D. A. Abanin, E. Altman, I. Bloch, and M. Serbyn, Colloquium : Many-body localization, thermalization, and entanglement, *Rev. Mod. Phys.* **91**, 021001 (2019).

[10] M. Schreiber, S. S. Hodgman, P. Bordia, H. P. Luschen, M. H. Fischer, R. Vosk, E. Altman, U. Schneider, and I. Bloch, Observation of many-body localization of interacting fermions in a quasirandom optical lattice, *Science* **349**, 842 (2015).

[11] D. Bluvstein, A. Omran, H. Levine, A. Keesling, G. Semeghini, S. Ebadi, T. T. Wang, A. A. Michailidis, N. Maskara, W. W. Ho, S. Choi, M. Serbyn, M. Greiner, V. Vuletic, and M. D. Lukin, Controlling many-body dynamics with driven quantum scars in rydberg atom arrays, *arXiv preprint arXiv:2012.12276* (2020).

[12] T. Brydges, A. Elben, P. Jurcevic, B. Vermersch, C. Maier, B. P. Lanyon, P. Zoller, R. Blatt, and C. F. Roos, Probing Rényi entanglement entropy via randomized measurements, *Science* **364**, 260 (2019).

[13] M. K. Joshi, A. Elben, B. Vermersch, T. Brydges, C. Maier, P. Zoller, R. Blatt, and C. F. Roos, Quantum Information Scrambling in a Trapped-Ion Quantum Simulator with Tunable Range Interactions, *Phys. Rev.*

Lett. **124**, 240505 (2020).

[14] A. Rubio-Abadal, M. Ippoliti, S. Hollerith, D. Wei, J. Rui, S. L. Sondhi, V. Khemani, C. Gross, and I. Bloch, Floquet Prethermalization in a Bose-Hubbard System, *Phys. Rev. X* **10**, 021044 (2020).

[15] D. Zhu, S. Johri, N. H. Nguyen, C. H. Alderete, K. A. Landsman, N. M. Linke, C. Monroe, and A. Y. Matsuru, Probing many-body localization on a noisy quantum computer, *arXiv preprint arXiv:2006.12355* (2020).

[16] X. Mi, *et.al*, Information scrambling in computationally complex quantum circuits, *arXiv preprint arXiv:2101.08870* (2021).

[17] H. Bernien, S. Schwartz, A. Keesling, H. Levine, A. Omran, H. Pichler, S. Choi, A. S. Zibrov, M. Endres, M. Greiner, V. Vuletić, and M. D. Lukin, Probing many-body dynamics on a 51-atom quantum simulator, *Nature* **551**, 579 (2017).

[18] S. Moudgalya, N. Regnault, and B. A. Bernevig, Entanglement of exact excited states of Affleck-Kennedy-Lieb-Tasaki models: Exact results, many-body scars, and violation of the strong eigenstate thermalization hypothesis, *Phys. Rev. B* **98**, 235156 (2018).

[19] C. J. Turner, A. A. Michailidis, D. A. Abanin, M. Serbyn, and Z. Papić, Weak ergodicity breaking from quantum many-body scars, *Nature Physics* **14**, 745 (2018).

[20] C.-J. Lin and O. I. Motrunich, Exact Quantum Many-Body Scar States in the Rydberg-Blockaded Atom Chain, *Phys. Rev. Lett.* **122**, 173401 (2019).

[21] M. Schecter and T. Iadecola, Weak ergodicity breaking and quantum many-body scars in spin-1 xy magnets, *Phys. Rev. Lett.* **123**, 147201 (2019).

[22] S. Sugiura, T. Kuwahara, and K. Saito, Many-body scar state intrinsic to periodically driven system: Rigorous results, *arXiv preprint arXiv:1911.06092* (2019).

[23] T. Iadecola, M. Schecter, and S. Xu, Quantum many-body scars from magnon condensation, *Phys. Rev. B* **100**, 184312 (2019).

[24] K. Lee, R. Melendrez, A. Pal, and H. J. Changlani, Exact three-colored quantum scars from geometric frustration, *Phys. Rev. B* **101**, 241111 (2020).

[25] A. J. James, R. M. Konik, and N. J. Robinson, Nonthermal States Arising from Confinement in One and Two Dimensions, *Phys. Rev. Lett.* **122**, 130603 (2019).

[26] S. Ok, K. Choo, C. Mudry, C. Castelnovo, C. Chamon, and T. Neupert, Topological many-body scar states in dimensions one, two, and three, *Phys. Rev. Research* **1**, 033144 (2019).

[27] H. Zhao, J. Vovrosh, F. Mintert, and J. Knolle, Quantum many-body scars in optical lattices, *Phys. Rev. Lett.* **124**, 160604 (2020).

[28] B. Mukherjee, S. Nandy, A. Sen, D. Sen, and K. Sengupta, Collapse and revival of quantum many-body scars via floquet engineering, *Phys. Rev. B* **101**, 245107 (2020).

[29] S. Moudgalya, N. Regnault, and B. A. Bernevig, η - pairing in Hubbard models: From spectrum generating algebras to quantum many-body scars, *Phys. Rev. B* **102**, 085140 (2020).

[30] C.-J. Lin, A. Chandran, and O. I. Motrunich, Slow thermalization of exact quantum many-body scar states under perturbations, *Phys. Rev. Research* **2**, 033044 (2020).

[31] S. Pai and M. Pretko, Dynamical Scar States in Driven Fracton Systems, *Phys. Rev. Lett.* **123**, 136401 (2019).

[32] P. Sala, T. Rakovszky, R. Verresen, M. Knap, and F. Pollmann, Ergodicity Breaking Arising from Hilbert Space Fragmentation in Dipole-Conserving Hamiltonians, *Phys. Rev. X* **10**, 011047 (2020).

[33] T. Rakovszky, P. Sala, R. Verresen, M. Knap, and F. Pollmann, Statistical localization: From strong fragmentation to strong edge modes, *Phys. Rev. B* **101**, 125126 (2020).

[34] V. Khemani, M. Hermele, and R. Nandkishore, Localization from hilbert space shattering: From theory to physical realizations, *Phys. Rev. B* **101**, 174204 (2020).

[35] Z.-C. Yang, F. Liu, A. V. Gorshkov, and T. Iadecola, Hilbert-Space Fragmentation from Strict Confinement, *Phys. Rev. Lett.* **124**, 207602 (2020).

[36] G. De Tomasi, D. Hetterich, P. Sala, and F. Pollmann, Dynamics of strongly interacting systems: From fock-space fragmentation to many-body localization, *Phys. Rev. B* **100**, 214313 (2019).

[37] L. Herviou, J. H. Bardarson, and N. Regnault, Many-body localization in a fragmented hilbert space, *arXiv preprint arXiv:2011.04659* (2020).

[38] O. Vafek, N. Regnault, and B. A. Bernevig, Entanglement of exact excited eigenstates of the Hubbard model in arbitrary dimension, *SciPost Physics* **3**, 043 (2017).

[39] K. Lee, A. Pal, and H. J. Changlani, Frustration-induced emergent hilbert space fragmentation, *arXiv preprint arXiv:2011.01936* (2020).

[40] S. Scherg, T. Kohlert, P. Sala, F. Pollmann, B. H. M., I. Bloch, and M. Aidelsburger, Observing non-ergodicity due to kinetic constraints in tilted Fermi-Hubbard chains, *arXiv preprint arXiv:2010.12965* (2020).

[41] S. Moudgalya, A. Prem, R. Nandkishore, N. Regnault, and B. A. Bernevig, Thermalization and its absence within krylov subspaces of a constrained hamiltonian, *arXiv preprint arXiv:1910.14048* (2019).

[42] J.-Y. Desaules, A. Hudomal, C. J. Turner, and Z. Papić, A proposal for realising quantum scars in the tilted 1d fermi-hubbard model, *arXiv preprint arXiv:2102.01675* (2021).

[43] O. Salberger and V. Korepin, Fredkin spin chain, *arXiv preprint arXiv:1605.03842* (2016).

[44] O. Salberger, T. Udagawa, Z. Zhang, H. Katsura, I. Klich, and V. Korepin, Deformed Fredkin spin chain with extensive entanglement, *Journal of Statistical Mechanics: Theory and Experiment* **2017**, 063103 (2017).

[45] Z. Zhang and I. Klich, Entropy, gap and a multi-parameter deformation of the fredkin spin chain, *Journal of Physics A: Mathematical and Theoretical* **50**, 425201 (2017).

[46] T. Udagawa and H. Katsura, Finite-size gap, magnetization, and entanglement of deformed fredkin spin chain, *Journal of Physics A: Mathematical and Theoretical* **50** (2017).

[47] R. Movassagh and P. W. Shor, Supercritical entanglement in local systems: Counterexample to the area law for quantum matter, *Proceedings of the National Academy of Sciences* **113**, 13278 (2016).

[48] N. Shiraishi and T. Mori, Systematic Construction of Counterexamples to the Eigenstate Thermalization Hypothesis, *Phys. Rev. Lett.* **119**, 030601 (2017).

[49] N. Shiraishi, Connection between quantum-many-body scars and the Affleck-Kennedy-Lieb-Tasaki model from the viewpoint of embedded Hamiltonians, *Journal of Statistical Mechanics: Theory and Experiment* **2019**, 083103 (2019).

[50] M. Schecter and T. Iadecola, Many-body spectral reflec-

tion symmetry and protected infinite-temperature degeneracy, *Phys. Rev. B* **98**, 035139 (2018).

[51] A. Pal and D. A. Huse, Many-body localization phase transition, *Phys. Rev. B* **82**, 174411 (2010).

[52] Y. Y. Atas, E. Bogomolny, O. Giraud, and G. Roux, Distribution of the Ratio of Consecutive Level Spacings in Random Matrix Ensembles, *Phys. Rev. Lett.* **110**, 084101 (2013).

[53] D. S. Rokhsar and S. A. Kivelson, Superconductivity and the quantum hard-core dimer gas, *Phys. Rev. Lett.* **61**, 2376 (1988).

[54] S. A. Kivelson, D. S. Rokhsar, and J. P. Sethna, Topology of the resonating valence-bond state: Solitons and high- T_c superconductivity, *Phys. Rev. B* **35**, 8865 (1987).

[55] X. Chen, E. Fradkin, and W. Witczak-Krempa, Gapless quantum spin chains: multiple dynamics and conformal wavefunctions, *Journal of Physics A: Mathematical and Theoretical* **50**, 464002 (2017).

[56] If the sequence only contains red(blue) particles, the effective Hamiltonian is positive(negative). Therefore $|\Psi(q)\rangle$ is the ground (ceiling) state in this case.

[57] M. Ljubotina, M. Žnidarič, and T. Prosen, A class of states supporting diffusive spin dynamics in the isotropic heisenberg model, *Journal of Physics A: Mathematical and Theoretical* **50**, 475002 (2017).

[58] J. Mossel and J.-S. Caux, Relaxation dynamics in the gapped xxz spin-1/2 chain, *New Journal of Physics* **12**, 055028 (2010).

[59] J. Haegeman, C. Lubich, I. Oseledets, B. Vandereycken, and F. Verstraete, Unifying time evolution and optimization with matrix product states, *Phys. Rev. B* **94**, 165116 (2016).

[60] J. Haegeman, J. I. Cirac, T. J. Osborne, I. Pižorn, H. Verschelde, and F. Verstraete, Time-dependent variational principle for quantum lattices, *Phys. Rev. Lett.* **107**, 070601 (2011).

[61] B. P. Lanyon, C. Hempel, D. Nigg, M. Müller, R. Gerritsma, F. Zahringer, P. Schindler, J. T. Barreiro, M. Rambach, G. Kirchmair, M. Hennrich, P. Zoller, R. Blatt, and C. F. Roos, Universal Digital Quantum Simulation with Trapped Ions, *Science* **334**, 57 (2011).

[62] R. Barends, L. Lamata, J. Kelly, L. García-Álvarez, A. Fowler, A. Megrant, E. Jeffrey, T. White, D. Sank, J. Mutus, *et al.*, Digital quantum simulation of fermionic models with a superconducting circuit, *Nature Communications* **6**, 7654 (2015).

[63] J. W. Britton, B. C. Sawyer, A. C. Keith, C.-C. J. Wang, J. K. Freericks, H. Uys, M. J. Biercuk, and J. J. Bollinger, Engineered two-dimensional Ising interactions in a trapped-ion quantum simulator with hundreds of spins, *Nature* **484**, 489 (2012).

[64] E. J. Zhang, S. Srinivasan, N. Sundaresan, D. F. Bogorin, Y. Martin, J. B. Hertzberg, J. Timmerwilke, E. J. Pritchett, J.-B. Yau, C. Wang, W. Landers, E. P. Lewandowski, A. Narasgond, S. Rosenblatt, G. A. Keefe, I. Lauer, M. B. Rothwell, D. T. McClure, O. E. Dial, J. S. Orcutt, M. Brink, and J. M. Chow, High-fidelity superconducting quantum processors via laser-annealing of transmon qubits, *arXiv preprint arXiv:2012.08475* (2020).

[65] J. W. P. Wilkinson, K. Klobas, T. Prosen, and J. P. Garrahan, Exact solution of the Floquet-PXP cellular automaton, *arXiv preprint arXiv:2006.06556* (2020).

[66] T. Iadecola and S. Vijay, Nonergodic quantum dynamics from deformations of classical cellular automata, *Phys. Rev. B* **102**, 180302 (2020).

[67] S. Gopalakrishnan and B. Zakirov, Facilitated quantum cellular automata as simple models with non-thermal eigenstates and dynamics, *Quantum Science and Technology* **3**, 044004 (2018).

[68] T. Kim and B.-S. Choi, Efficient decomposition methods for controlled-r n using a single ancillary qubit, *Scientific reports* **8**, 1 (2018).

[69] T. Ono, R. Okamoto, M. Tanida, H. F. Hofmann, and S. Takeuchi, Implementation of a quantum controlled-swap gate with photonic circuits, *Scientific reports* **7**, 1 (2017).

[70] M.-S. Kang, J. Heo, S.-G. Choi, S. Moon, and S.-W. Han, Optical fredkin gate assisted by quantum dot within optical cavity under vacuum noise and sideband leakage, *Scientific reports* **10**, 1 (2020).

[71] F. M. Gambetta, C. Zhang, M. Hennrich, I. Lesanovsky, and W. Li, Long-range multibody interactions and three-body antiblockade in a trapped rydberg ion chain, *Phys. Rev. Lett.* **125**, 133602 (2020).

[72] W. Feng and D.-w. Wang, Quantum fredkin gate based on synthetic three-body interactions in superconducting circuits, *Phys. Rev. A* **101**, 062312 (2020).

[73] F. Petziol, M. Sameti, S. Carretta, S. Wimberger, and F. Mintert, Quantum simulation of three-body interactions in weakly driven quantum systems, *arXiv preprint arXiv:2011.03399* (2020).

Appendix A: Controlled-SWAP Spin Moves and Mapping Spins to Particles

In this section we first discuss how the destructive interference arises and then outline how to develop the color ordered configurations. Recall that the spin moves of the Hamiltonian, Eq. (1) perform a controlled-SWAP operation on three-spin sequence as follows, $|\uparrow\uparrow\downarrow\rangle \longleftrightarrow |\uparrow\downarrow\uparrow\rangle$ and $|\downarrow\uparrow\downarrow\rangle \longleftrightarrow -|\uparrow\downarrow\downarrow\rangle$. Due to the destructive interference of the two spin moves, the allowed spin moves on four-spins are

$$|\uparrow\uparrow\downarrow\downarrow\rangle \longleftrightarrow |\uparrow\downarrow\uparrow\uparrow\rangle \quad |\downarrow\downarrow\uparrow\downarrow\rangle \longleftrightarrow -|\downarrow\uparrow\downarrow\downarrow\rangle \quad (A1)$$

As a result, the domain-wall and Néel states are eigenstates of the Hamiltonian. As a demonstration consider the domain-wall state, $|\uparrow\uparrow\cdots\uparrow\downarrow\downarrow\cdots\downarrow\downarrow\rangle$. According to the map, this state becomes: $|\uparrow\uparrow\cdots\uparrow\downarrow\downarrow\cdots\downarrow\downarrow\rangle - |\uparrow\uparrow\cdots\downarrow\uparrow\downarrow\cdots\downarrow\downarrow\rangle$, which clearly cancels. This interfering behavior prevents sub-sectors from being connected that otherwise are in the standard Fredkin model.

Due to the destructive interference of the spin moves, each sub-sector carries a domain-wall number accompanied by a $U(1)$ charge, which become manifest through an effective particle-hole mapping. Each sub-sector is characterized by a color string of particles with an imposed kinetic constraint of disallowed particle exchange. The set of all spin states that map to the same color sequence construct a fragmented sub-sector of the Hilbert space. In order to determine these sequences from a given state we apply the steps discussed below.

Given a spin state in the full Hilbert space first we map every sequence, $(\downarrow\uparrow) \rightarrow \circ$, denoted as a hole. Then every individual remaining spin becomes a color particle, $\downarrow(\uparrow) \rightarrow \bullet(\bullet)$. The unique label for the sub-sector is found by removing all the holes, leaving a colored string where the order of particle color must be maintained. The spin moves in this picture correspond now to a particles hopping through a hole background. However, there are certain sequences when an immobility arises. These possibilities are summarized as, (i) $\cdots\bullet\bullet\circ\bullet\cdots$, (ii) $|\circ\bullet\bullet\cdots$, (iii) $\cdots\bullet\circ|$, where $|\$ stands for the boundary. The holes in the above configurations are immobile due to conservation of n_{dw} and S_z . More generally, if there are multiple holes in the above configurations, a single immobile hole will be left after hopping. We demonstrate this with the following example.

Consider the state, $\downarrow\downarrow\uparrow\uparrow\downarrow\downarrow\uparrow\uparrow\uparrow\uparrow$. First, we replace each two-spin sequence, $(\downarrow\uparrow)$, with, \circ . Our state now becomes, $\downarrow\downarrow\circ\circ\circ\uparrow\uparrow$. Now map the remaining individual spins to colored particles resulting in the state, $\bullet\bullet\circ\circ\circ\bullet\bullet\bullet$. Consider the sequence of the blue particle hopping to the right, $\bullet\bullet\circ\circ\circ\bullet\bullet\bullet \rightarrow \bullet\circ\bullet\circ\circ\bullet\bullet\bullet \rightarrow \bullet\circ\bullet\circ\circ\bullet\bullet\bullet$. Notice that the final part, $\cdots\bullet\circ\bullet\bullet$, the hole can no longer propagate without violating domain-wall and charge number, therefore, to ensure the symmetries are conserved we need to remove a single hole. The sub-sector is then formed by $n_\bullet = n_\bullet = 2$ with $n_\circ = 2$, where the color ordered string is $\bullet\bullet\bullet\bullet$. Consequently, these immobile particles are inert in otherwise nearest-neighbor hopping. Therefore, each spin sequence after the map has immobile particles and boundaries that begin(end) with $\bullet(\bullet)$ removed. After these degrees of freedom are taken into account the final configuration is composed of, n_\bullet , n_\circ and mobile holes n_\circ that label a fragmented sub-sector.

Appendix B: Entanglement Entropy for Exact Eigenstate

In Eq. (5) of the main text, we construct an exact eigenstate for each invariant sub-sector of the Hamiltonian Eq. (3). To calculate the half-chain entanglement entropy of this state, we first perform a Schmidt-decomposition with the cut placed in the center of the chain

$$|\Psi\rangle = \sum_i \lambda_i |\Psi_i^L\rangle |\Psi_i^R\rangle, \quad (B1)$$

where $|\Psi_i^{R/L}\rangle$ is a set of orthonormal states on the left(right) half of the chain and the λ_i is the Schmidt coefficient. Due to the normalization of $|\Psi\rangle$, the Schmidt coefficients obey $\sum \lambda_i^2 = 1$. From λ_i , the Rényi entropy of index α can be calculated as

$$S^{(\alpha)} = \frac{1}{1-\alpha} \log \sum_i \lambda_i^{2\alpha}. \quad (B2)$$

Because of the wavefunctions factorable structure and the conserved number of holes, the orthonormal basis, $|\Psi^{L(R)}\rangle$, can be labelled by the number of holes on each side. Therefore the Schmidt decomposition is re-written as

$$|\Psi\rangle = \sum_m \lambda_m |\Psi_m^L\rangle |\Psi_{n_\circ-m}^R\rangle \quad (B3)$$

where m is the hole number on the left, and $n_\circ - m$ is the hole number on the right. Note that m can be both integer and half-integer, the half-integers correspond to the case where the entanglement cut is through a hole which takes two site in the spin representation. The number of holes on the left(right) side is between 0 and $N/4$, imposing a constraint on the range of m ,

$$\begin{cases} 0 \leq m \leq n_\circ, & n_\circ \leq \frac{N}{4} \\ n_\circ - \frac{N}{4} \leq m \leq \frac{N}{4}, & n_\circ > \frac{N}{4} \end{cases} \quad (\text{B4})$$

As a result, there are at most $\min(2n_\circ + 1, N - 2n_\circ + 1)$ nonzero singular values. The entanglement entropy is therefore upper bounded by $S \leq \log(\min(2n_\circ + 1, N - 2n_\circ + 1))$. However, when either $n_\bullet + n_\circ$ or n_\circ stays finite as $N \rightarrow \infty$, the exact state has area-law entanglement entropy. When n_\circ/N stays fixed as $N \rightarrow \infty$, the entanglement scales as $\log(N)$ or remains area law depending on values of q , which is elaborated on below. In any case, however, the state has sub-volume law entanglement, violating ETH.

In order to obtain the entanglement scaling for the case when n_\circ increases linearly with N , we look into the Schmidt decomposition Eq. (B3) more closely. The states $|\Psi_m^L\rangle$ are,

$$|\Psi_m^L\rangle = \frac{1}{\mathcal{N}_m(q)} \exp(-\log(q)\hat{\mathcal{P}}_L/2) \sum_m |\psi_m^L\rangle. \quad (\text{B5})$$

The summation is over all states on the left partition containing m holes, and $\mathcal{N}_m(q)$ is the normalization factor. The state $|\Psi_m^R\rangle$ is similarly constructed,

$$|\Psi_m^R\rangle = \frac{1}{\mathcal{N}_m(q)} \exp(-\log(q)\hat{\mathcal{P}}_R/2) \sum_m |\psi_m^R\rangle. \quad (\text{B6})$$

The Schmidt coefficients are

$$\lambda_m(q) = \frac{\mathcal{N}_m(q)\mathcal{N}_{n_\circ-m}(q)}{\mathcal{N}(q)}. \quad (\text{B7})$$

We now provide the explicit derivation of the Rényi entropy for the exact state with the sub-sector labeled by $\bullet\bullet\cdots\bullet\bullet\cdots\bullet\bullet$ with $n_\bullet = n_\circ$ in the large N limit. Due to the fixed boundaries, $n_\bullet + n_\circ = N/2 - 1$. As we will show below, the large N scaling of the Rényi entropy depends on whether $q = 1$, $q < 1$ or $q > 1$.

1. Case of $q = 1$

When $q = 1$ the exact eigenstate is an equal weight superposition independent of the dipole moment. As a result the normalization factor, $\mathcal{N}(q)^2 = \text{tr}(q^{-\hat{\mathcal{P}}}) = \dim$ which can be found using combinatorial methods. We find the total Hilbert space dimension and the dimension of each half with fixed hole number to be

$$\mathcal{N}^2 = \binom{2n_\bullet + n_\circ}{2n_\bullet}, \quad \mathcal{N}_m^2 = \binom{\lfloor -m \rfloor + n_\circ + n_\bullet}{\lfloor m \rfloor} \quad (\text{B8})$$

where $\lfloor \cdots \rfloor$ is the floor function. When m is a half-integer, it implies that a hole ($\downarrow\uparrow$) is in the middle of chain. The Schmidt coefficients λ can be computed straightforwardly

$$\lambda_m^2 = \binom{\lfloor -m \rfloor + n_\circ + n_\bullet}{\lfloor m \rfloor} \binom{\lfloor m \rfloor - n_\circ}{\lfloor n_\circ - m \rfloor} \Big/ \binom{2n_\bullet + n_\circ}{2n_\bullet} \quad (\text{B9})$$

Then the Rényi entropy before taking the log is

$$\exp((1 - \alpha)S^{(\alpha)}) = \sum_m \lambda_m^{2\alpha} = \sum_m \left(\binom{n_\bullet + n_\circ + \lfloor -m \rfloor}{\lfloor m \rfloor} \right)^\alpha \left(\binom{\lfloor m \rfloor + n_\bullet}{n_\circ + \lfloor -m \rfloor} \right)^\alpha \Big/ \left(\binom{2n_\bullet + n_\circ}{2n_\bullet} \right)^\alpha \quad (\text{B10})$$

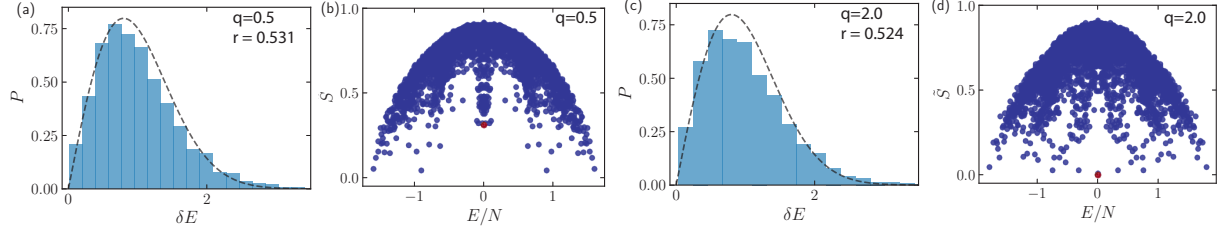


FIG. 5. (a) and (c) Level spacing between adjacent eigenvalues for the color sequence, $\bullet\bullet\bullet\bullet\bullet\bullet\bullet$, with $n_o = 10$ and $\text{dim} = 8008$. The distribution is found by resolving the spectral-symmetry and then using a small energy window of the remaining spectrum. The inset gives the deformation value and average level ratio parameter, $\langle r \rangle$. (b) and (d) Normalized half-chain entanglement entropy, \tilde{S} , for the same sub-sector using exact diagonalization. For $q = 0.5$ a majority of the eigenstates form an ETH band but the presence of outlying states remain visible. In the regime, $q = 2.0$, the ETH band begins to collapse and further scarring is observed. The red point is the entanglement for the exact eigenstate, Eq. (5) with $\tilde{S} \sim 0$.

The Rényi entropy can be calculated in the thermodynamic limit, $N \rightarrow \infty$. We further set $\alpha = 2$ and obtain

$$S^{(2)} = \begin{cases} 2n_o \log 2 - \log \binom{2n_o}{n_o} & \text{if } N \rightarrow \infty \text{ and } n_o \ll N \\ 4n_\bullet \log 2 - \log \binom{4n_\bullet}{2n_\bullet} & \text{if } N \rightarrow \infty \text{ and } n_\bullet \ll N \\ \frac{1}{2} \log(N) + \frac{1}{2} \log(\pi(1-\gamma)(2-\gamma)\gamma) - \log((1-\gamma)^2 + 1) & \text{if } N \rightarrow \infty \text{ and } \gamma = n_o/N \text{ finite} \end{cases} \quad (\text{B11})$$

As expected, S exhibits area law when either n_o or n_\bullet stay fixed as $N \rightarrow \infty$ and scales logarithmically with N if the ratio n_o/N remains fixed instead. In the following sections we determine the behavior away from the critical point.

2. Case of $q > 1$

We now consider the Rényi entropy when the deformation $q > 1$, where we are interested in the regime with $\gamma = n_o/N$ fixed as $N \rightarrow \infty$. In this case, the exact eigenstate is a superposition of all states in the computational basis weighted by the its dipole moment. The largest contribution is from the state of largest dipole moment, given by

$$|\bullet\bullet\cdots\bullet\overbrace{\circ\cdots\circ}^{n_o}\bullet\cdots\bullet\rangle. \quad (\text{B12})$$

The states with $\gamma N - \mathcal{O}(1)$ holes between the two color domains have the same dipole moment density as Eq. (B12), and contribute to the exact state. Similarly, other states have a small density, $|\hat{\mathcal{P}}|$ and are exponentially suppressed by large N . The contributing states have identically half the number of holes on each half of the chain. As a result, the Schmidt coefficient λ_m is 1 when $m = n_o/2$ and 0 otherwise. This suggests that for $q > 1$ and $N \rightarrow \infty$ the entanglement entropy for the exact state vanishes. When N is finite the entanglement decays to zero rapidly as q increases from 1.

We confirm this behavior numerically using MPS for $N = 100$ to 400 in Fig. 2(b). This behavior can also be seen in Fig. 5(d) where the entanglement entropy for the exact state (red point) is approximately zero. An interesting direction would be to study the critical regime, $(q-1) \sim 1/N$.

3. Case of $q < 1$

In this case the entanglement entropy has area or logarithmic scaling depending on the ratio, $\gamma = n_o/N$. We consider the same sub-sector with $n_\bullet = n_\circ$ with $q < 1$ and finite in the large N limit. Here the superposition will be

dominated by a uniform superposition of states minimizing the dipole moment amplitude,

$$\frac{1}{n_o + 1} \sum_{m=0}^{n_o} |\underbrace{\bullet \circ \cdots \circ}_{m} \cdots \bullet \cdots \bullet \cdots \bullet \circ \cdots \circ \bullet \rangle \quad (\text{B13})$$

for $0 \leq m \leq n_o$. Unlike the previous case, there is no unique state but a $(n_o + 1)$ dimensional manifold of states. Now let us consider the half-chain entanglement entropy for the uniform superposition of these states in the spin representation. When $n_\bullet \geq n_o$ or equivalently $\gamma \leq 1/4$, the particle domain $\bullet \cdots \bullet \bullet \cdots \bullet$ takes more than half of the chain. As a result, the half-chain cut intersects the particle domain for each of the $(n_o + 1)$ configurations. Therefore the states $\Psi^{R/L}$ from the Schmidt decomposition are

$$|\Psi_m^L\rangle = |\underbrace{\bullet \circ \cdots \circ}_{m} \bullet \cdots \rangle, \quad |\Psi_{n_o-m}^R\rangle = |\cdots \bullet \circ \cdots \circ \bullet \rangle \quad (\text{B14})$$

where m range from 0 to n_o . Therefore, the state Eq. (B13) in this case has a flat entanglement spectrum with $(n_o + 1)$ Schmidt coefficients. The half chain entanglement entropy is just $\log(n_o + 1)$, which scales as, $\gamma \log(N)$.

When $n_\bullet < n_o$ or $\gamma > 1/4$, the cut is within the hole domain for some of the configurations, for which the entire particle domain is within the left side or the right side. Therefore, one half of the chain is frozen and the corresponding Schmidt decomposition becomes,

$$\begin{aligned} |\Psi_{(n_o+n_\bullet)/2}^L\rangle &= |\underbrace{\bullet \circ \cdots \circ}_{(n_o+n_\bullet)/2} \rangle, \quad |\Psi_{(n_o-n_\bullet)/2}^R\rangle = \frac{1}{(n_o - n_\bullet)/2 + 1} \sum_{m=0}^{(n_o-n_\bullet)/2} |\underbrace{\circ \cdots \circ}_{m} \bullet \cdots \bullet \cdots \bullet \circ \cdots \circ \bullet \rangle \\ |\Psi_{(n_o+n_\bullet)/2}^R\rangle &= |\underbrace{\circ \cdots \circ}_{(n_o+n_\bullet)/2} \bullet \rangle, \quad |\Psi_{(n_o-n_\bullet)/2}^L\rangle = \frac{1}{(n_o - n_\bullet)/2 + 1} \sum_{m=0}^{(n_o-n_\bullet)/2} |\underbrace{\bullet \circ \cdots \circ}_{m} \bullet \cdots \bullet \cdots \bullet \circ \cdots \circ \bullet \rangle \end{aligned} \quad (\text{B15})$$

The Schmidt coefficients associated with the two pairs of state are

$$\lambda^2 = \frac{(n_o - n_\bullet)/2 + 1}{n_o + 1} \quad (\text{B16})$$

We have assumed $n_o + n_\bullet$ is an even number for simplicity. In addition, there are another $n_\bullet - 1$ pairs of states similar to those in Eq. (B14) with the same Schmidt coefficients $\lambda^2 = 1/(n_o + 1)$. From these Schmidt coefficients, we obtain the Rényi entropy for $\gamma > 1/4$ in the thermodynamic limit as

$$S = 2 \log(4\gamma) - 2 \log(4\gamma - 1) - \log 2 \quad (\text{B17})$$

which clearly has no dependence on the chain length demonstrating area law behavior.

Appendix C: The Matrix Product Representation of the Exact Eigenstate

In order to study the entanglement structure of the exact eigenstate we construct a matrix product ansatz in the spin representation. Each sub-sector hosts an exact eigenstate with zero energy density which is a weighted superposition of each basis state and therefore sits in the middle of the spectrum and has the form

$$|\Psi(q)\rangle = \frac{1}{\mathcal{N}} \mathbf{P} \left(q^{-\hat{\mathcal{P}}/2} \sum_{i=1}^{2^N} |\psi\rangle_i \right) \quad (\text{C1})$$

where \mathbf{P} projects the state into the invariant sub-sector designated by the color sequence with the normalization factor, \mathcal{N} . Our task is to construct an exact MPS for the state

$$|\Psi(q)\rangle = \sum_{\{s\}} A_1^{s_1} A_2^{s_2} \cdots A_N^{s_N} |s_1 s_2 \cdots s_N\rangle \quad (\text{C2})$$

here the matrices A_i^s are to be determined. The summation in Eq. (C1) is over the entire Hilbert space, which allows the state before the projection to be decomposed as a product state

$$q^{-\hat{\mathcal{P}}/2} \sum_{i=1}^{2^N} |\psi\rangle_i = \prod_{i=1}^N \left(q^{-i/2} |\uparrow\rangle_i + q^{i/2} |\downarrow\rangle_i \right). \quad (\text{C3})$$

Therefore, the difficulty of constructing the MPS depends on the correct matrix product operator for the projection, \mathbf{P} . Once obtained the exact eigenstate follows. The structure of the projection operator depends on the sub-sector defined through the color sequence. Generically, the projection operator is defined as

$$\mathbf{P} = \sum_i^{\dim} |\psi_i\rangle \langle \psi_i| \quad (\text{C4})$$

where the sum is now over the states in the fragmented sub-sector. Using standard techniques we seek the projection as a matrix product operator(MPO) of the form

$$\mathbf{P} = V_L^T \mathbb{P}_1 \mathbb{P}_2 \cdots \mathbb{P}_N V_R \quad (\text{C5})$$

where \mathbb{P}_i is a $d \times d$ matrix of local operators living on site i , where d is the bond dimension of the MPO. V_L and V_R are d -dimensional boundary vectors to ensure that the result is an operator.

The MPO can be constructed by induction: we require that

$$V_L^T \prod_1^r \mathbb{P}_i = (\mathbf{P}_r(0), \mathbf{P}_r(1/2), \mathbf{P}_r(1), \cdots \mathbf{P}_r(n_o)) \quad (\text{C6})$$

where $\mathbf{P}_r(n)$ is the projection operator acting on the first r sites to ensure that the states contain n holes after mapping. The projection operator, $\mathbf{P}_r(n)$, can be obtained by combining $\mathbf{P}_{r-1}(n)$, $\mathbf{P}_{r-1}(n-1/2)$ and the operators defined on site r . The combination, which depends on the color sequence, specifies the matrix operator, \mathbb{P}_r . To be concrete, consider the sub-sector given by $\bullet\bullet\cdots\bullet\bullet\cdots\bullet\bullet$. We have the following iteration rules

$$\begin{aligned} \mathbf{P}_r(n+1/2) &= \mathbf{P}_{r-1}(n) P_r^\downarrow \\ \mathbf{P}_r(n) &= \begin{cases} \mathbf{P}_{r-1}(n-1/2) P_r^\uparrow + \mathbf{P}_{r-1}(n) P_r^{\sigma(r-2n)}, & 2n_o - 2n < N - r \\ \mathbf{P}_{r-1}(n-1/2) P_r^\uparrow, & 2n_o - 2n \geq N - r \end{cases} \end{aligned} \quad (\text{C7})$$

The site index r goes from 2 to $N-1$. When $r=1$, $\mathbf{P}_1(n) = P_1^\uparrow \delta_{n,0}$ and the first spin is fixed to be up. When $r=N$, $\mathbf{P}_N(n_o) = \mathbf{P}_{N-1}(n_o) P_N^\downarrow$ and the last spin is fixed to be down. From the iteration rules, one can construct the MPO accordingly. The naive maximal bond dimension of the MPO constructed using this approach is $2n_o + 1$. However, at a given site, not all $2n_o + 1$ projectors $\mathbf{P}_r(n)$ are physical because the constraint that the n holes has to fit into r sites and the remaining $n_o - n$ holes has to fit into the remaining $N - r - 1$ sites. Following the iteration rules given above, the non physical projectors becomes 0, leading to reduction of the bond dimension. One can show that the maximal bond dimension in this case is $\min(2n_o + 1, n_\bullet)$. The MPO of the projection operator for other sub-sectors can be constructed in a similar manner. With the MPO of the projection operator, one can immediately obtain the MPS of the exact eigenstate by acting on the product state Eq. (C3).

Appendix D: MPO of the Hamiltonian and Details on Simulating the Dynamics

In this section, we write down the MPO of the Hamiltonian in Eq. (3), which is used in standard TDVP algorithm to evolve matrix product states. The Hamiltonian is

$$H = \frac{4}{q} \sum_{i=1}^{N-2} P_{i-1}^\uparrow |\Phi(q)\rangle \langle \Phi(q)|_{i,i+1} - |\Phi(q)\rangle \langle \Phi(q)|_{i,i+1} P_{i+2}^\downarrow \quad (\text{D1})$$

where the un-normalized state is defined as, $|\Phi(q)\rangle_{i,i+1} = |\uparrow\rangle_i |\downarrow\rangle_{i+1} - q |\downarrow\rangle_i |\uparrow\rangle_{i+1}$. It is convenient to re-express the two site projectors in terms of Pauli operators

$$\frac{4}{q} |\Phi(q)\rangle \langle \Phi(q)|_{i,i+1} = \frac{4}{q} P_i^\uparrow P_{i+1}^\downarrow + 4q P_i^\downarrow P_{i+1}^\uparrow - 2 (\sigma_i^x \sigma_{i+1}^x + \sigma_i^y \sigma_{i+1}^y). \quad (\text{D2})$$

We would like to convert the Hamiltonian to a matrix product operator

$$H = V_L^T \mathbb{H}_1 \mathbb{H}_2 \cdots \mathbb{H}_N V_R \quad (\text{D3})$$

where \mathbb{H}_i is a matrix of operators defined on each site and $V_{L/R}$ are boundary vectors. The MPO is used as the input for the tensor network simulation of the dynamics. Following the standard approach, one can show that

$$V_L = (1, 0, 0, 0, 0, 0)^T, \quad V_R = (0, 0, 0, 0, 0, 1)^T, \quad \mathbb{H}_i = \begin{pmatrix} I_i & P_i^\uparrow & 0 & \vec{O}_{L,i}^T & 0 & 0 \\ 0 & 0 & \vec{O}_{L,i}^T & 0 & 0 & 0 \\ 0 & 0 & 0 & 0 & 0 & \vec{O}_{R,i} \\ 0 & 0 & 0 & 0 & \vec{O}_{R,i} & 0 \\ 0 & 0 & 0 & 0 & 0 & -P_i^\downarrow \\ 0 & 0 & 0 & 0 & 0 & I_i \end{pmatrix} \quad (\text{D4})$$

where

$$\vec{O}_{L,i} = \left(\frac{4}{q} P_i^\uparrow, 4q P_i^\downarrow, -4\sigma_i^x, -4\sigma_i^y \right)^T, \quad \vec{O}_{R,i} = \left(P_i^\downarrow, P_i^\uparrow, \sigma_i^x, \sigma_i^y \right)^T \quad (\text{D5})$$

so that $\vec{O}_{L,i}^T \vec{O}_{R,i} = \frac{4}{q} |\Phi(q)\rangle \langle \Phi(q)|_{i,i+1}$. The bond dimension of the MPO is 12. One can check that

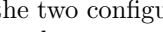
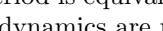
$$V_L^T \prod_i^N \mathbb{H}_i = \left(\mathbb{1}, P_N^\uparrow, P_{N-1}^\uparrow \vec{O}_{L,N}^T, \vec{O}_{L,N}^T, O_{N-1,N}, H \right) \quad (\text{D6})$$

which multiplied by the right boundary vector gives the Hamiltonian. This completes the construction of the MPO for the Hamiltonian and we now discuss how unitary evolution using the time-dependent variational algorithm(TDVP) [59, 60].

The TDVP-MPS algorithm has the advantage to explicitly conserve the energy of the state during time evolution, and therefore is particularly suitable for simulating dynamics governed by a time independent Hamiltonian. However, the TDVP does not respect the emergent conserved color sequence. Consequently, the algorithm can introduce a state that does not belong to the fragmented sub-sector introducing error. In order to mitigate the probability of this occurring, we combine the MPO of the Hamiltonian with the projection operator discussed in Sec. C, and use the MPO of H in the TDVP simulation.

Appendix E: Dynamics and Eigenstate Properties

In this section we study the eigenstate entanglement entropy and dynamics through exact diagonalization for a pair of deformation values, $(q, 1/q)$. We first checked that over the range, $q \in [0.5, 2.0]$, the level statistics remain Wigner-Dyson, illustrated in Fig. 5(a) and (c). In Fig. 5(b) and (d) we determine the eigenstate bipartite entanglement entropy in the sub-sector defined by,  with $n_\circ = 10$. For $q < 1.0$ there is a distinct ETH band, however, the quantum many-body scars persist. At $q > 1$ the distribution of entanglement begins to collapse and broaden, but weakly entangled states far below the band are apparent.

To accompany the TDVP-MPS simulations we perform exact diagonalization in the spin representation within the same sub-sector and compute the time evolution of the operator expectation, $\langle \sigma_i^z(t) \rangle$. Illustrated in Fig. 6 the system is quenched upon being prepared in the large(small) dipole state. Since the domains are small the timescale over which the boundary term becomes important is short. As explained in the main text, due to the boundary term, the energy difference between the two configurations  and  is $V(q) - h(q) = 4q$ instead of $V(q) = 2(1/q + q)$. As a result, the boundary term reduces the energy cost of detaching the domain from the boundary for $q < 1$, causing ballistic domain propagation. The collisions of the two domains contribute to the entanglement oscillations in Fig. 2(d), where the period is equivalent to the timescale between the domain scattering, Fig. 6(a). For the large dipole state at $q = 2.0$ the dynamics are nearly stationary because the boundary term increases the energy cost to move the domain. Recall that Hamiltonian at $q = 0.5$ and $q = 2.0$ only differ by the boundary term. For the small dipole state shown in Fig. 6, the red domain oscillates for both $q = 0.5$ and $q = 2.0$. This follows because when the red domain detached the blue domain,  the nearest-neighbor energy from the  and  contribute an energy $V(q)$ and $-V(q)$ which cancel, ensuring the net energy at zero. Due to this cancellation the holes between the two domains act as an effective boundary by maintaining the energy allowing the red domain to collectively propagate. On the other hand, the dynamics of the blue domain is affected by the boundary term. We also check that random product states in the fractured sub-sector obey Krylov-ETH and thermalize in a short time scale, Fig. 6(c).

In Fig. 7 we simulate the effective Hamiltonian, Eq. (4) using exact diagonalization with and without the boundary term to explicitly demonstrate its effect. We focus on two cases that exhibit long time coherent oscillation: (a)

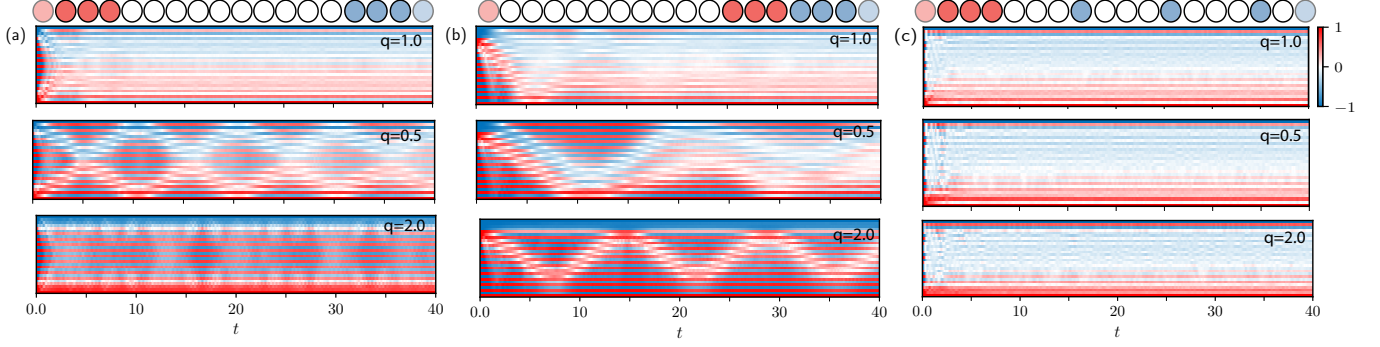


FIG. 6. (a-c) Dynamics of $\langle \sigma_i^z(t) \rangle$ from exact diagonalization for $q = 1.0, 0.5, 2.0$ prepared in the state with (a) large dipole amplitude (b) small dipole amplitude and (c) a random state. The non-ergodic dynamics are apparent in (a) and (b) at $q = 0.5$ ($q = 2.0$) where coherent oscillations are present corresponding to particle scattering. While at $q = 2.0$ in (a) the dynamics are nearly static since the prepared state is approximately an eigenstate. (c) Demonstrates the quench dynamics with a random state, for which thermalization occurs across all deformation values.

$|\bullet\bullet\cdots\bullet\circ\cdots\circ\bullet\cdots\bullet\rangle$ at $q = 0.5$, (b) $|\bullet\circ\cdots\circ\bullet\cdots\bullet\circ\cdots\bullet\rangle$ at $q = 2.0$. In the first case shown in Fig. 7(a) when there is no boundary term the dynamics are nearly static due to the boundary term no longer minimizing the energy cost to move the domains. A different behavior arises in Fig. 7(b) where coherent oscillations persist in the absence of the boundary.

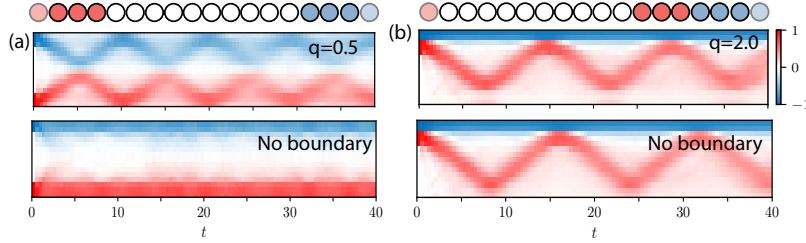


FIG. 7. (a-b) Dynamics of $\langle n_{i,\bullet}(t) \rangle - \langle n_{i,\circ}(t) \rangle$ using exact diagonalization of the effective Hamiltonian, Eq. (4). The parameters are $N = 28$ with the color sequence $\bullet\bullet\cdots\bullet\circ\cdots\circ\bullet\cdots\bullet$ and $n_\circ = 10$ for $t = 40$ with a time step, $dt = 0.05$. The bottom panels are the effective Hamiltonian with the boundary term removed. When the system is quenched from the state with the smallest dipole amplitude in the absence of the boundary non-ergodic behavior still persists. This follows from the nearest-neighbor energy cancelling between the red(blue) domain, as a result, the holes induce an effective boundary allowing the red domain to collectively propagate.

Appendix F: Floquet Unitary Circuit

Here we provide details for an efficient gate decomposition for the Floquet circuit for arbitrary ξ and q given in Eq. 6, shown in Fig. 8. The three-site gate is decomposed into a series of CNOT gate and single-site gate $H(q)$ and $R(q, \xi)$ where

$$H(q) = \frac{1}{\sqrt{1+q^2}}(qI + i\sigma^y), \quad R(\xi, q) = \exp\left(-i\frac{\xi(1+q^2)}{2q}\sigma^z\right) = \exp\left(-i\frac{\pi}{4}\frac{\xi}{\xi_o(q)}\sigma^z\right) \quad (\text{F1})$$

When $q = 1$, $H(q)$ becomes the Hadamard gate, and when $\xi = \xi_o/2$, $R(q, \xi)$ becomes the T gate. At $\xi = \pi/8$ and $q = 1$, the three-site gate becomes the Fredkin gate. Recent advancements in quantum dots and photonic circuits has made experimental realization of this gate attainable [68–73]. Through these experimental methods the discussed fragmentation structure and resulting non-ergodic dynamics is feasible in the imminent future utilizing near term intermediate scale quantum devices.

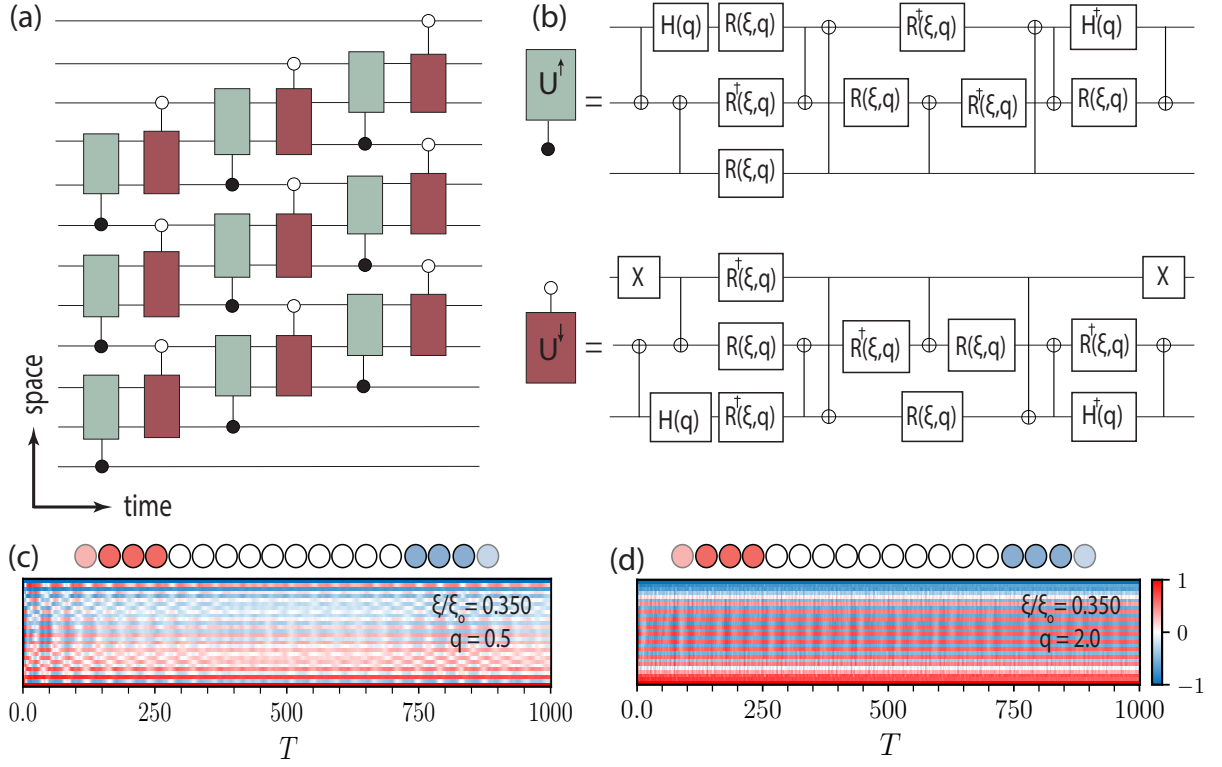


FIG. 8. (a) Quantum circuit diagram of the Floquet operator consisting of six layers each containing three-site gates. The circles represent the control-bit with the filled getting projected on by $|\uparrow\rangle\langle\uparrow|$ and the empty by $|\downarrow\rangle\langle\downarrow|$. (b) Efficient gate decomposition into CNOT and on-site gates. (c-d) Quench dynamics of the Floquet operator from the state with the large dipole amplitude in the sub-sector generated by $n_\bullet = n_\circ = 3$ and $n_o = 10$ for 1000 periods. The circuit is evaluated at $(\xi/\xi_o = 0.350, q = 0.5)$ in (c) and $(\xi/\xi_o = 0.350, q = 2.0)$ in (d). Note that the stationary behavior still persists for $q > 1.0$, while for $q < 1.0$ there are coherent oscillations indicating the non-ergodic dynamics remain present.